Skyrmion Hall effect revealed by direct time-resolved X-ray microscopy

Kai Litzius[1,2,3], Ivan Lemesh[4], Benjamin Krüger[1], Pedram Bassirian[1], Lucas Caretta[4], Kornel Richter[1], Felix Büttner[4], Koji Sato[5], Oleg A. Tretiakov[6,7], Johannes Förster[3], Robert M. Reeve[1], Markus Weigand[3], Iuliia Bykova[3], Hermann Stoll[3], Gisela Schütz[3], Geoffrey S. D. Beach[4]* and Mathias Kläui[1,2]*

Magnetic skyrmions are promising candidates for future spintronic applications such as skyrmion racetrack memories and logic devices. They exhibit exotic and complex dynamics governed by topology and are less influenced by defects, such as edge roughness, than conventionally used domain walls. In particular, their non-zero topological charge leads to a predicted 'skyrmion Hall effect', in which current-driven skyrmions acquire a transverse velocity component analogous to charged particles in the conventional Hall effect. Here, we use nanoscale pump–probe imaging to reveal the real-time dynamics of skyrmions driven by current-induced spin–orbit torques. We find that skyrmions move at a well-defined angle Θ_{SkH} that can exceed 30° with respect to the current flow, but in contrast to conventional theoretical expectations, Θ_{SkH} increases linearly with velocity up to at least 100 ms^{-1}. We qualitatively explain our observation based on internal mode excitations in combination with a field-like spin–orbit torque, showing that one must go beyond the usual rigid skyrmion description to understand the dynamics.

In most magnetic materials, the exchange interaction is symmetric, favouring a collinear alignment of spins. However, recently a new type of magnetic system with broken inversion symmetry has moved to the focus of modern solid-state physics. In such systems, the interfacial Dzyaloshinskii–Moriya interaction (DMI)[1,2] favours a perpendicular alignment of adjacent spins, and its interplay with the symmetric exchange interaction then leads to a helical spin structure with well-defined handedness[3–9]. One of the most interesting spin structures that originates in this type of material is the magnetic skyrmion[3,4,10,11]. This topologically non-trivial, particle-like structure exhibits very interesting properties, such as topological stabilization and predicted efficient current-induced motion[12–15]. One major advantage is that skyrmions experience a repulsive force from geometrical boundaries such as the edges of a magnetic track. This is in contrast to ordinary domain walls, which are strongly affected by edge roughness. As a result, skyrmions interact less with geometrical irregularities and are expected to move smoothly and with high stability along the track. In combination with an efficient driving mechanism, such as spin–orbit torques[16–18], this makes them promising candidates for future applications, where fast and reliable switching is key[19,20]. However, during current-induced displacements, skyrmions have been predicted to exhibit an effect that is similar to the Hall effect for electrons, and is therefore called the skyrmion Hall effect. As a result, the current not only induces longitudinal but also transversal motion of the skyrmions, which has to be considered especially in logic gates[20]. The skyrmion Hall effect plays an important role in the dynamics of skyrmions because it can change the transversal position of the skyrmion within the track, and therefore lead to the annihilation of the skyrmion quasi-particle at the edge. Since skyrmions at rest are expected always to be centred in the track due to the edge repulsion, quasi-static imaging can lead, in particular in low-pinning systems, to incorrect determination of the skyrmion Hall angle. Only direct dynamic imaging of the displacement in real time can reveal the dynamic velocities and displacement direction to understand and tailor the skyrmion motion in devices.

In this work, we perform pump–probe X-ray microscopy thatreveals the real-space trajectories and dynamic velocities of individual skyrmions in a magnetic racetrack. Our results demonstrate that the necessary reproducibility and uniformity of the motion for time-resolved measurements of current-induced dynamics excited by spin–orbit torques (SOTs) is indeed realized in our optimized stack structure, showing the applicability for devices. We observe a large skyrmion Hall angle and find a strong dependence on the skyrmion velocity that cannot be explained by standard micromagnetic simulations that include only the conventionally used damping-like (DL)-SOT[16]. We find that micromagnetic predictions qualitatively reproduce a drive dependence of the skyrmion Hall angle when including field-like (FL)-SOTs. This result suggests that the FL-SOT plays a more important role than expected so far, and we explain the observations based on excitations of the skyrmion spin structure that go beyond the previously assumed rigid skyrmion description of the dynamics.

To reveal the interplay between FL and DL torques and their influence on the resulting skyrmion dynamics, we used an optimized low-pinning stack based on thin multilayers of

[1]Institute of Physics, Johannes Gutenberg University Mainz, 55099 Mainz, Germany. [2]Graduate School of Excellence Materials Science in Mainz, 55128 Mainz, Germany. [3]Max Planck Institute for Intelligent Systems, 70569 Stuttgart, Germany. [4]Department of Materials Science and Engineering, Massachusetts Institute of Technology, Cambridge, Massachusetts 02139, USA. [5]WPI Advanced Institute for Materials Research, Tohoku University, Sendai 980-8577, Japan. [6]Institute for Materials Research, Tohoku University, Sendai 980-8577, Japan. [7]School of Natural Sciences, Far Eastern Federal University, Vladivostok 690950, Russia. *e-mail: gbeach@mit.edu; klaeui@uni-mainz.de

$[Pt(3.2\,nm)/CoFeB(0.7\,nm)/MgO(1.4\,nm)]_{15}$. The contrast between very high DMI at the Pt/CoFeB interface and the lower DMI at the CoFeB/MgO interface results in a large net DMI; additionally, the materials composition yields a strong perpendicular magnetic anisotropy (PMA). Together, these are able to stabilize magnetic skyrmions in the stack at room temperature, as previously shown in ref. 17. Furthermore, this material exhibits excellent homogeneity—resulting in a landscape with a very low pinning energy—and thus has great potential for obtaining reliable skyrmion dynamics. In particular, the reproducibility of skyrmion motion resulting from low pinning is crucial for pump–probe dynamic measurements that reveal the dynamic velocities. Since the experimental contrast is integrated over billions of repetitions of the excitation process, variations in the skyrmion trajectories due to stochastic processes would not yield a clear signal. The schematics of the measurement can be found in Fig. 1.

First, we determine the topological properties and average velocities of the skyrmions, which identify the observed spin structures as chiral skyrmions[13,21]. As already introduced in ref. 17, we used the dependence of the skyrmion trajectory on the DMI to determine the chirality of the system. The direction of the SOT-driven motion of the skyrmion along the track ($\pm x$) depends only on the sign of the DMI constant D, for a given spin Hall angle, and is independent of the skyrmion polarity. We find that the skyrmion motion occurs against the electron flow direction, which is the characteristic behaviour for left-handed Néel domain walls and skyrmions, as expected for Pt-interface-based materials when Pt is the bottom interface. Having established the topological properties, we turn to the dynamics in more detail. First we apply an out-of-plane magnetic field of 30 mT to set the size of the skyrmions[11,17]. A typical view of such a skyrmion and a fit of its out-of-plane magnetization profile can be found in Fig. 2a,b. Note that the analysis takes into account the convolution with the X-ray beam, which increases the observed contrast diameter as compared to the real skyrmion diameter. The skyrmion diameter shown in the figure represents the apparent skyrmion size during the dynamics. To excite the dynamics, we applied bipolar current pulses designed to drive the skyrmions back and forth to restore the initial state after each pump–probe cycle. This allows for time-resolved imaging where each frame corresponds to a snapshot of the skyrmions during the measurement cycle, and therefore also during the excitation (details in Methods).

Previous work demonstrated high average skyrmion velocities exceeding 100 ms^{-1} at current densities around 5×10^{11} A m^{-2}, enabled by the low pinning in this material[17]. However, that work relied on static imaging of the skyrmion positions before and after current-pulse application, without providing information on the dynamic trajectories and velocities. Pump–probe measurements, by contrast, provide access to dynamic (time-resolved) velocity profiles of the skyrmions, which cannot be directly inferred from conventional static measurements because material inhomogeneities (for example, pinning sites) can significantly influence the dynamic trajectory and velocities. For this type of measurement, a tailored excitation is required so that the pulses always move the skyrmions reproducibly between the same positions. Details on this requirement and the resulting effects for the skyrmion dynamics can be found in Supplementary Section 2. Furthermore, only dynamic imaging can reveal the open question of the effective mass and the inertia, as previously found to be sizeable for bubble skyrmions[13]. Therefore, as a first step, we extract the dynamic velocities of the skyrmions as a function of time. This can be done by tracking the skyrmion positions in each frame of the pump–probe measurement and then calculating the displacements within the given time between the frames. Since our samples are placed on thin silicon nitride membranes in vacuum, the heat dissipation is poor. For this reason, we include an increased delay between the unipolar pulses with positive and negative polarity

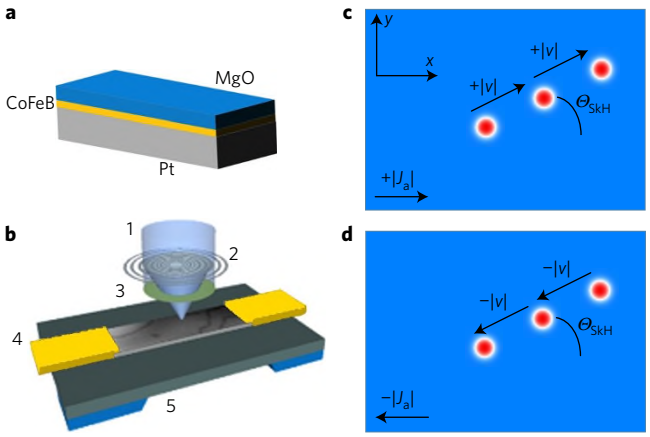

Figure 1 | Schematic description of technique and observed skyrmion Hall effect. a, Observed stack as single repetition. The layers show the relative experimental thickness differences. **b**, Schematics of the scanning transmission X-ray microscopy (STXM) measurements. An X-ray beam (1) is focused via a zone plate (2) and an aperture (3) on the sample (4), which is contacted by two gold striplines. The beam is transmitted through the sample and the silicon nitride membrane (5). On the other side (not shown), the beam is detected. The transmission of X-rays depends on the magnetization at the specific focus spot. **c**,**d**, Skyrmions moving in a magnetic wire (micromagnetic simulations, red and blue correspond to negative and positive out-of-plane contrast, respectively). When excited by an alternating current, the skyrmions move backwards and forwards at a specific angle with respect to the current flow direction, the skyrmion Hall angle Θ_{SkH}.

to allow the system to cool down (in the Supplementary Movie we omit the frames corresponding to this delay period to highlight the important times during the pulse injection where the dynamics occur). Figure 2c shows the time-resolved skyrmion velocity. It can be seen that the velocity follows the current density without any noticeable delay, implying that the observed skyrmions exhibit only a small inertia (upper bound $\approx 1.3 \times 10^{-21}$ kg), which is significantly lower than the values measured in ref. 13, where the inertia was found to be large for non-chiral bubble skyrmions. This can be explained as derived in ref. 13: the skyrmion mass scales inversely with the rigidity of the spin structure, which in our case is very high because of the strong DMI. The DMI lowers the effective mass, because it makes the spin structure more rigid, and thus counteracts the deformations needed for generating the effective mass. As a result, the mass of our skyrmions can be expected to be small as compared to the non-chiral bubble skyrmions observed in ref. 13, which is in line with the observations and in agreement with our micromagnetic simulations showing a delay of <100 ps and a very similar response as compared to the experimental observations (Supplementary Fig. 4). We note that different uses of the term 'bubble skyrmion' are found in literature. Our use of the term (as previously introduced in ref. 17), means that a 'bubble' describes a magnetic structure with little DMI, and therefore is used for skyrmions that are not necessarily chiral. Sometimes one can read the term 'bubble skyrmion' also for skyrmions with a plateau region in their centre, however this is not necessarily a feature set by the DMI value. One can obtain a plateau for skyrmions in materials with different combinations of DMI and anisotropy and in general the model described within this work can be used for a range of DMI values as long as the skyrmion is chiral, as is the case for the material used here where a fully Néel type domain wall is present.

The extracted peak dynamic velocities are slightly higher than the averaged ones in the current density versus velocity plots derived from static measurements[17]. This effect stems from the unknown threshold current density in the static imaging and the dynamic

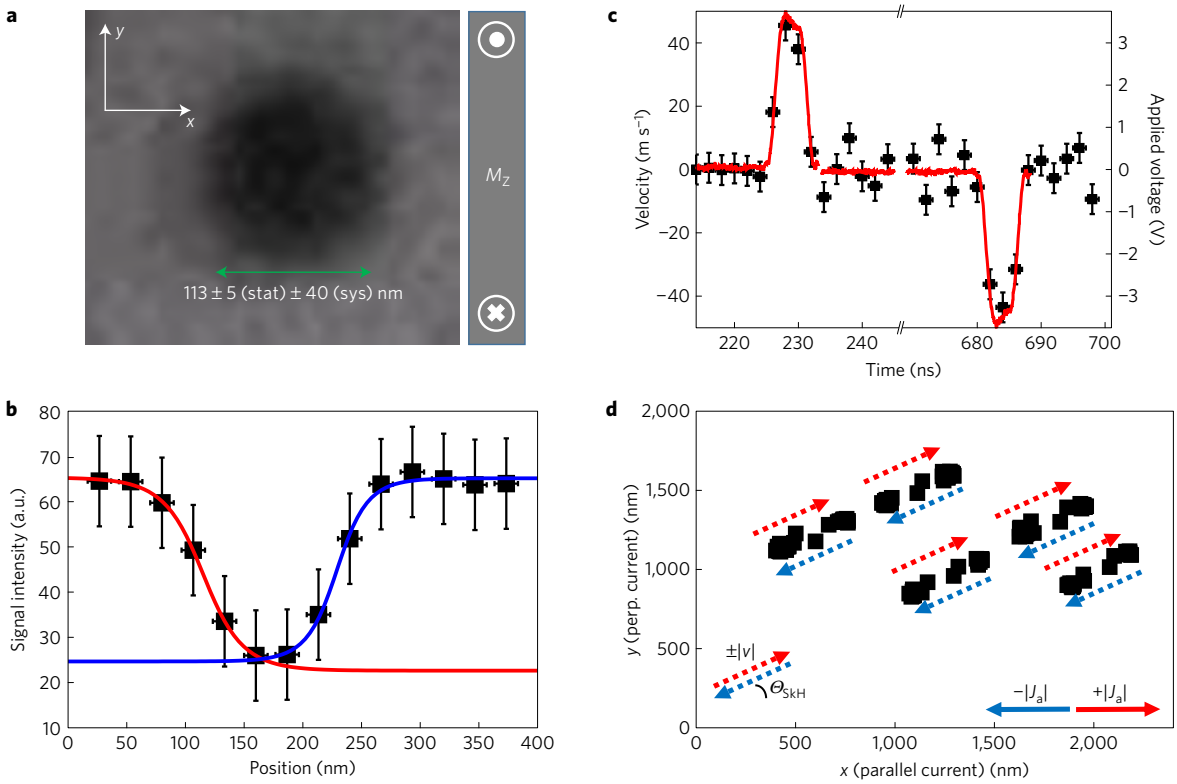

Figure 2 | Analysis of skyrmions and skyrmion trajectories. a,**b**, Image of a typical skyrmion as seen by STXM imaging with the size indicated (excited size during the dynamics) (**a**) and fitted profile (**b**). The error bars of position and signal, respectively, are given by half a pixel spatial resolution and the standard deviation of the profile calculated from all the frames where the skyrmion is stationary. The fits of both walls were carried out using the equation $\Theta_{DW}(x, c, \Delta) = 2\arctan(\exp((x-c)/\Delta))$, which describes a Néel wall at position c with width Δ (refs 10,23). The resulting domain wall width of 15 nm is in line with micromagnetic simulations. **c**, Dynamic velocity as a function of time (black) with the applied voltage pulse (red). The error bar is given by the uncertainty of the skyrmion centre position. No visible delay implies low inertia, and thus a low effective mass. **d**, Skyrmion trajectories for one experimental current density (4.2×10^{11} A m^{-2}). All skyrmions move in parallel and synchronously. Furthermore, the skyrmions move reproducibly, showing that our pulses are well-tailored to obtain identical displacements for positive and negative pulses, as needed for pump–probe measurements. The vertical range of 2 μm corresponds to the width of the used wire.

velocity versus current-density dependence that only dynamic imaging is able to reveal. Comparing the width of the pulse and the width of the response, one can see that the absolute amount of time the skyrmions move due to the current pulse (~6 ns) is comparable to the full-width at half-maximum (FWHM) value of the excitation itself, while the shapes fit the expected ones from simulations very well (Supplementary Fig. 4). This means the skyrmions move very efficiently, with velocities reaching those predicted for perfect, pinning-free, systems. The knowledge of the exact velocity as a function of current density is especially important for short current pulses with non-rectangular shape. In this case, the skyrmions do not move with the velocities expected from averaged current-density values, and therefore will end up at a different location in the track, which can be predicted only by knowing the dynamic velocities that we reveal here.

Next, we use dynamic imaging to study the skyrmion properties during the dynamics, which is completely inaccessible by conventional quasi-static measurements (see also Supplementary Sections 2 and 3). Micromagnetic simulations predict that the skyrmion can change its size; in particular, above a threshold current density, the skyrmion size is predicted to increase significantly and continuously during its motion. This can significantly alter the skyrmion's behaviour and, since it shrinks back to its equilibrium size after several nanoseconds, cannot be detected without dynamic imaging. For our current densities, our experiment reveals no significant difference of the size due to the current excitation, showing that the skyrmions exhibit stable dynamics.

Finally, we analyse the skyrmion trajectory and compare the direction of the motion to the applied current flow direction. To do this we plot parallel and perpendicular components of the trajectories of several skyrmions visible within the scanning transmission X-ray microscopy (STXM) field of view, where the current flow is directed along the x axis. The trajectories are shown for one of the different experimentally investigated current densities (4.2×10^{11} A m^{-2}) (Fig. 2d). The parallel trajectories of several freely moving skyrmions are clearly visible, indicating fully reproducible motion without significant influence from pinning (otherwise the pump–probe measurements, which combine over 10^9 repetitions of the dynamic process, would show only noise due to stochastic motion). All skyrmion trajectories show the same constant angle with respect to the current flow direction for the same current density, which is a hallmark of the skyrmion Hall effect.

Surprisingly, our experimental data collected for several current densities show a pronounced dependence of the skyrmion Hall angle on the skyrmion velocity, as shown in Fig. 3. This is in contrast to previous micromagnetic simulations[22], as well as analytical models of rigid skyrmion motion driven by a damping-like torque[16], which predict a velocity-independent skyrmion Hall angle Θ_{SkH} of about $\tan\Theta_{SkH} = G/\alpha\tilde{D}$, where G is the gyrovector, α is the damping parameter, and $\tilde{D}$ is the dissipation factor[16]. For a skyrmion whose radius R is much larger than the domain wall width Δ, one can show that $\tan\Theta_{SkH} \approx \pm 2\Delta/\alpha R$ using the analytical expression for the skyrmion spin texture in ref. 23. With $\alpha = 0.5$ and $\Delta \approx 15$ nm (estimated from our material parameters

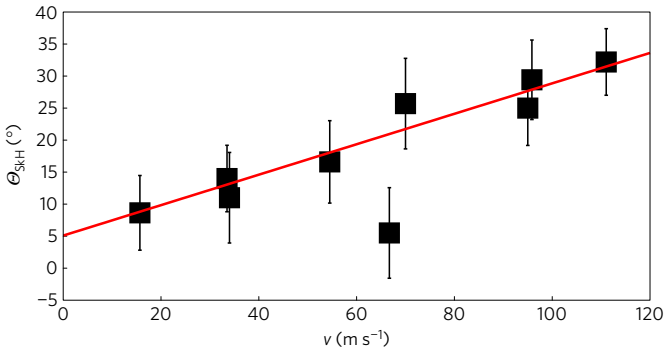

Figure 3 | Experimentally observed skyrmion Hall angles of the skyrmion displacement with respect to the current flow direction for different velocities. When plotted as a function of the extracted dynamic peak velocities of the observed angles, a linear dependence is found. This is consistent for all samples, even with different pinning properties (different threshold current densities to move the skyrmions), implying that pinning cannot be the only origin of this behaviour. The error bars of the angles are given by the uncertainty of the skyrmion centre position. The linear fit (red line) is a guide for the eye.

and consistent with micromagnetic simulations as well as with a fit of the experimental data (Fig. 2) with the corresponding model for Δ) conventional models predict a velocity-independent $\Theta_{SkH} \sim 60°$. This analytical estimate is in good agreement with our micromagnetic results based on DL-SOT using the same material parameters. Here, we used the experimentally observed skyrmion diameter of ∼110 nm as an upper bound for the skyrmion size. As a rule of thumb, one can expect an apparent broadening of the domains by up to ∼35 nm due to the partially coherent zone plate illumination. Additionally, drift in the z-direction can change the focus, thus leading to a change of the apparent diameter. Together, these effects can result in an increased skyrmion diameter, leading to an uncertainty in the estimated Θ_{SkH}. The assumed value for the damping parameter, α, reflects the enhanced damping expected due to the Pt/CoFeB interfaces in stray-field-coupled Pt/ferromagnet multilayers[24–26]. We note that the skyrmion Hall angle estimated using the rigid skyrmion model described above should serve as a lower limit, in that a lower assumed value of damping or a larger assumed value of the domain wall width would result in an even larger expected skyrmion Hall angle.

Experimentally, the absolute values of the skyrmion Hall angles are smaller than the analytical and micromagnetic predictions based on the parameters described above, and we find a linear dependence of Θ_{SkH} on the velocity (current density), as seen in Fig. 3. The trend that the skyrmion Hall angle depends on the velocity is visible for nominally identical skyrmions such that the dependence can be ascribed to the dynamics rather than different skyrmion spin structures. These behaviours cannot be explained by conventional micromagnetic simulations including only a DL-SOT. In addition, for reasonable changes of material parameters such as the DMI constant, saturation magnetization M_s or damping parameter, which could give an increased error bar (see Supplementary Fig. 5), we also cannot explain the behaviour (see Supplementary Section 4) at the experimental current densities. We note that during the preparation of this manuscript, we became aware of a related static observation of the skyrmion Hall angle as a function of current density and a corresponding theoretical work[27,28] showing qualitatively a similar trend at low current densities that could originate from pinning.

We conclude further that there must be an additional, intrinsic effect, which is influencing the skyrmion trajectories. We have studied possible scenarios that can explain this increase of the observed angles with increasing skyrmion velocity. One parameter, which has previously been neglected, is the sizeable field-like (FL)-SOT that has been observed in these multilayer materials. Its influence can be quantified by the field-like parameter ξ, which is the ratio of the FL and DL torque. So far, only rigid skyrmions or skyrmions that deform only slightly and excitations with a simplified DL-SOT have been considered. In this case, simulations and the Thiele equation (for details see Supplementary Section 6) assuming a fully rigid skyrmion predict no influence of the FL-SOT on the skyrmion trajectories at all. However, additional degrees of freedom that allow the skyrmion to deform slightly and breathe[29] can lead to an influence of a FL-SOT as we show here (Fig. 4, more details in Supplementary Figs 6 and 7). Together with a non-simplified SOT with DL and FL components[30,31] we find a sizeable influence of the FL-SOTs: an increasing current and thus an increasing FL-SOT changes the skyrmion Hall angle (Fig. 4). It furthermore affects faster skyrmions to a greater extent than slower ones because the former are less rigid and thus more susceptible to this effect. To support this argument, we also study the dependence of the skyrmion Hall angle on the diameter of the observed skyrmions at rest between the applied pulses. As shown in Fig. 5, the experimentally observed skyrmion Hall angles at constant skyrmion velocity decrease with increasing size of the skyrmions. This inverse dependence of the skyrmion Hall angle on skyrmion size is qualitatively consistent with the rigid skyrmion model and can contribute an offset to the velocity–Hall angle dependence. However, when fitting the rigid skyrmion model estimation for the skyrmion Hall angle (model A in Fig. 5), one obtains an unphysically small ratio between domain wall width and damping constant $\Delta/\alpha = (7.6 \pm 1.0)$ nm. This means that the rigid skyrmion model alone is not sufficient to explain the observed effects. A slight modification of the model, however, can shed light on the effect. We add an offset to the equation $\Theta_{SkH} \approx \mathrm{atan}(2\Delta/(\alpha R)) + c$, which is the simplest approximation to account for the additional effect of the skyrmion deformation and the effect of the FL-SOT (motivated by micromagnetic simulations). The used fit can be applied with the already mentioned estimates for DW width $\Delta \approx 15$ nm and $\alpha = 0.5$, yielding an offset of $c \approx -(31 \pm 1)°$ and a much better agreement with the measured skyrmion Hall angles (model B in Fig. 5). This provides another indication that the usually applied rigid skyrmion model is not complete and an additional effect, such as the proposed deformations in the skyrmion profile by a field-like torque, can notably affect the skyrmion Hall angle.

Although the calculated and observed trend of increasing skyrmion Hall angles due to increasing skyrmion velocity agree qualitatively, quantitative agreement has not yet been obtained. This can be attributed to thermal excitations and size variations of the skyrmions due to varying material parameters as well as a stronger effective damping in the multilayer stack. Those effects increase the skyrmion deformation, change the offset of the skyrmion Hall angles or, in the case of the skyrmion size, alter the Hall angle directly. In particular, the thermal effects are not taken into account in the zero-temperature simulations, calling for future theoretical efforts beyond the scope of this work. However, we point out that the field-like SOT indeed can influence the skyrmion Hall angle, even in the complete absence of pinning, because of the deformation of the skyrmion spin structure itself. Up to now, a full analysis of the experimental spin structure including in-plane and out-of-plane components has not been possible due to a lack of dynamic imaging techniques with sufficiently high resolution that can image in the deep-sub-10 nm regime. Nevertheless, the introduced theoretical model offers a new approach to describe skyrmion dynamical behaviours that elude existing models, and provide concepts that are qualitatively in line with our observations.

This new aspect of the complex skyrmion dynamics provides an additional handle for tailoring the dynamic properties and, in combination with the highly reproducible dynamics, we have demonstrated that the developed Pt/CoFeB/MgO multilayer stack exhibits skyrmions that are suitable for spintronics applications.

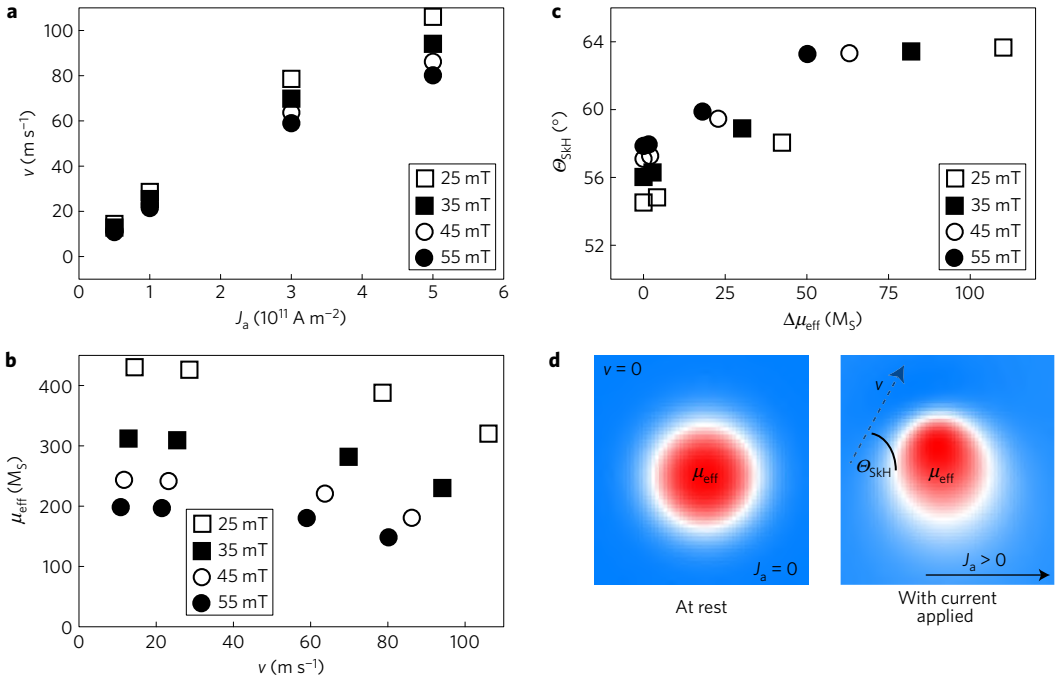

Figure 4 | The FL-SOT as the origin of the varying skyrmion Hall angle simulated with DL- and FL-SOTs ($\xi = 5$) at different out-of-plane fields. **a**, Dependence of the skyrmion velocity on the current density. **b**, Dependence of the total magnetic moment μ_{eff} of the skyrmion (effectively its size) on the velocity. μ_{eff} is defined as the average z-component of the magnetization inside the skyrmion, where inside the skyrmion is defined as the area enclosed by the ring of fully in-plane-oriented spins ($\mu_{eff} = \sum_{i|M_{z,i}<0} |M_{z,i}|$, where $M_{z,i}$ is the z-component of the magnetization in cell i and M_S is the saturation magnetization). In this particular case, the skyrmion size decreases slightly with increasing velocity. The change of skyrmion size is also accompanied by a deformation of its shape, and can therefore be seen as a measure of this deformation (see **d**). **c**, Dependence of the skyrmion Hall angle on the skyrmion's total magnetic moment, showing an increase with increasing deformation (plotted as the difference $\Delta\mu_{eff}$ between the moment (size) at rest and the corresponding value with applied current, given by $\Delta\mu_{eff} = |\mu_{eff}(J=0) - \mu_{eff}(J\neq 0)|$). This indicates that the Hall angle of the skyrmion trajectory is indeed affected by the skyrmion distortion, and therefore by the velocity. **d**, Micromagnetic simulation showing a typical distortion of the skyrmion shape due to the applied current. Although the overall area is not strongly affected, the shape, and therefore the diameter, of the inner region does change.

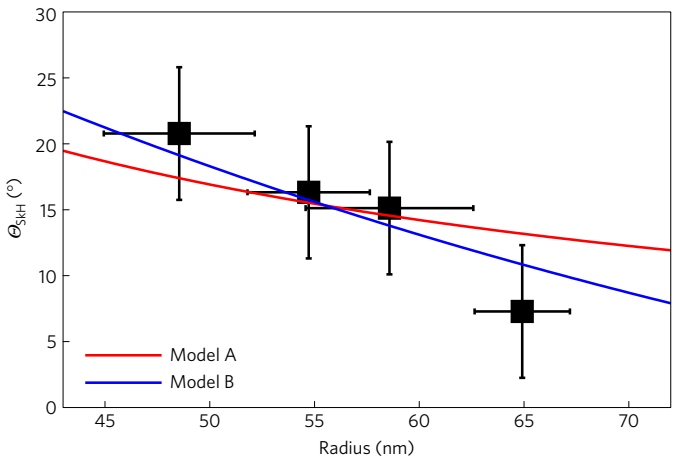

Figure 5 | Experimentally observed skyrmion Hall angles of the skyrmion displacement with respect to the current flow direction for different skyrmion diameters at constant skyrmion velocity. The general trend follows the rigid skyrmion approximation; however, a fit of the rigid model (model A) yields an unphysically small ratio of the domain wall over the damping ratio of $\Delta/\alpha = 7.6 \pm 1.0$ nm. At our estimated value for the damping (which is already relatively large), we would obtain a DW width of ~3.9 nm, and at lower α the result would get even more unrealistic. However, if we fit the data points with our expected DW width of 15 nm, damping 0.5, and add an offset that accounts for the influence of a deformation (model B) we achieve a much better agreement between fit and data. Error bars of radius and angle result from the obtained spatial resolution and the uncertainty of the skyrmion centre position, respectively.

Methods

Methods, including statements of data availability and any associated accession codes and references, are available in the online version of this paper.

References

1. Dzyaloshinsky, I. A thermodynamic theory of 'weak' ferromagnetism of antiferromagnetics. *J. Phys. Chem. Solids* **4,** 241–255 (1958).
2. Moriya, T. Anisotropic superexchange interaction and weak ferromagnetism. *Phys. Rev.* **120,** 91–98 (1960).
3. Rößler, U. K., Bogdanov, A. N. & Pfleiderer, C. Spontaneous skyrmion ground states in magnetic metals. *Nature* **442,** 797–801 (2006).
4. Mühlbauer, S. *et al*. Skyrmion lattice in a chiral magnet. *Science* **323,** 915–919 (2009).
5. Yu, X. Z. *et al*. Real-space observation of a two-dimensional skyrmion crystal. *Nature* **465,** 901–904 (2010).
6. Yu, X. Z. *et al*. Near room-temperature formation of a skyrmion crystal in thin-films of the helimagnet FeGe. *Nat. Mater.* **10,** 106–109 (2011).
7. Heinze, S. *et al*. Spontaneous atomic-scale magnetic skyrmion lattice in two dimensions. *Nat. Phys.* **7,** 713–718 (2011).
8. Uchida, M. *et al*. Real-space observation of helical spin order. *Science* **311,** 359–361 (2006).
9. Bode, M. *et al*. Chiral magnetic order at surfaces driven by inversion asymmetry. *Nature* **447,** 190–193 (2007).
10. Boulle, O. *et al*. Room-temperature chiral magnetic skyrmions in ultrathin magnetic nanostructures. *Nat. Nanotech.* **11,** 449–454 (2016).
11. Moreau-Luchaire, C. *et al*. Additive interfacial chiral interaction in multilayers for stabilization of small individual skyrmions at room temperature. *Nat. Nanotech.* **11,** 444–448 (2016).
12. Sampaio, J. *et al*. Nucleation, stability and current-induced motion of isolated magnetic skyrmions in nanostructures. *Nat. Nanotech.* **8,** 839–844 (2013).

13. Büttner, F. *et al*. Dynamics and inertia of skyrmionic spin structures. *Nat. Phys.* **11,** 225–228 (2015).
14. Rosch, A. Skyrmions: moving with the current. *Nat. Nanotech.* **8,** 160–161 (2013).
15. Iwasaki, J., Mochizuki, M. & Nagaosa, N. Current-induced skyrmion dynamics in constricted geometries. *Nat. Nanotech.* **8,** 742–747 (2013).
16. Tomasello, R. *et al*. A strategy for the design of skyrmion racetrack memories. *Sci. Rep.* **4,** 6784 (2014).
17. Woo, S. *et al*. Observation of room temperature magnetic skyrmions and their current-driven dynamics in ultrathin Co films. *Nat. Mater.* **15,** 501–506 (2016).
18. Jiang, W. *et al*. Blowing magnetic skyrmion bubbles. *Science* **349,** 283–286 (2015).
19. Fert, A., Cros, V. & Sampaio, J. Skyrmions on the track. *Nat. Nanotech.* **8,** 152–156 (2013).
20. Zhang, X. *et al*. Magnetic skyrmion logic gates: conversion, duplication and merging of skyrmions. *Sci. Rep.* **5,** 9400 (2015).
21. Malozemoff, A. P. & Slonczewski, J. C. *Magnetic Domain Walls in Bubble Materials* (Academic, 1979).
22. Nagaosa, N. & Tokura, Y. Topological properties and dynamics of magnetic skyrmions. *Nat. Nanotech.* **8,** 899–911 (2013).
23. Romming, N. *et al*. Field-dependent size and shape of single magnetic skyrmions. *Phys. Rev. Lett.* **114,** 177203 (2015).
24. Yuan, S. J. *et al*. Interfacial effects on magnetic relaxation in Co/Pt multilayers. *Phys. Rev. B* **68,** 134443 (2003).
25. Metaxas, P. J. *et al*. Creep and flow regimes of magnetic domain-wall motion in ultrathin Pt/Co/Pt films with perpendicular anisotropy. *Phys. Rev. Lett.* **99,** 217208 (2007).
26. Shellekens, A. J. *et al*. Determining the Gilbert damping in perpendicularly magnetized Pt/Co/AlO_x films. *Appl. Phys. Lett.* **102,** 082405 (2013).
27. Jiang, W. *et al*. Direct observation of the skyrmion Hall effect. *Nat. Phys.* http://dx.doi.org/10.1038/nphys3883 (2016).
28. Reichhardt, C. & Reichhardt, C. J. O. Noise fluctuations and drive dependence of the skyrmion Hall effect in disordered systems. *New J. Phys.* **18,** 095005 (2016).
29. Schütte, C. & Garst, M. Magnon-skyrmion scattering in chiral magnets. *Phys. Rev. B* **90,** 094423 (2014).
30. Qui, X. *et al*. Angular and temperature dependence of current induced spin–orbit effective fields in Ta/CoFeB/MgO nanowires. *Sci. Rep.* **4,** 4491 (2014).
31. Hayashi, M. *et al*. Quantitative characterization of the spin–orbit torque using harmonic Hall voltage measurements. *Phys. Rev. B* **89,** 144425 (2014).

Acknowledgements

Work at MIT was primarily supported by the US Department of Energy (DOE), Office of Science, Basic Energy Sciences (BES) under Award #DE-SC0012371 (sample fabrication). G.S.D.B. acknowledges support from C-SPIN, one of the six SRC STARnet Centers, sponsored by MARCO and DARPA. M.K. and the group at Mainz acknowledge support by the DFG (in particular SFB TRR173 Spin+X), the Graduate School of Excellence Materials Science in Mainz (MAINZ, GSC 266), the EU (MultiRev (ERC-2014-PoC 665672), MASPIC (ERC-2007-StG 208162), WALL (FP7-PEOPLE-2013-ITN 608031)), SpinNet, a topical network project of the German Academic Exchange Service (DAAD), and the Research Center of Innovative and Emerging Materials at Johannes Gutenberg University (CINEMA). M.K. thanks ICC-IMR at Tohoku University for their hospitality during a visiting researcher stay at the Institute for Materials Research. B.K. is grateful for financial support by the Carl-Zeiss-Foundation. F.B. acknowledges financial support by the German Research Foundation through grant no. BU 3297/1-1. O.A.T. acknowledges support by the Grants-in-Aid for Scientific Research (Grants No. 25800184, No. 25247056, and No. 15H01009) from the Ministry of Education, Culture, Sports, Science and Technology (MEXT) of Japan and SpinNet. K.L. gratefully acknowledges financial support by the Graduate School of Excellence Materials Science in Mainz (MAINZ) and the help and advice of Karin Everschor-Sitte and technicians of the Kläui group, especially S. Kauschke. Measurements were carried out at the MAXYMUS end station at Helmholtz-Zentrum Berlin. We thank HZB for the allocation of beamtime. Parts of this research were conducted using the supercomputer Mogon offered by Johannes Gutenberg University Mainz (hpc.uni-mainz.de), which is a member of the AHRP and the Gauss Alliance e.V.

Author contributions

M.K. and G.S.D.B. proposed and supervised the study. I.L. and K.L. fabricated devices. I.L. performed the film characterization. K.L., L.C., K.R., P.B., J.F., R.M.R., H.S., G.S., I.B. and M.W. conducted STXM experiments on the MAXYMUS beamline at the BESSY II synchrotron in Berlin. K.L. and M.K. performed and analysed the micromagnetic simulations. B.K., K.S. and O.A.T. derived a Thiele equation to explain the micromagnetic simulations and provided input for the latter. K.L., P.B. and K.R. performed the analytical analysis of the experimental data. F.B. derived the expression for the skyrmion Hall angle as a function of the domain wall width. All authors participated in the discussion and interpreted results. K.L. drafted the manuscript with the help of M.K. and assistance from G.S.D.B. All authors commented on the manuscript.

Additional information

Supplementary information is available in the online version of the paper. Reprints and permissions information is available online at www.nature.com/reprints. Correspondence and requests for materials should be addressed to G.S.D.B. or M.K.

Competing financial interests

The authors declare no competing financial interests.

Methods

We have grown multilayer films of $[Pt(3.2\,nm)/CoFeB(0.7\,nm)/MgO(1.4\,nm)]_{15}$ using d.c. and radiofrequency magnetron sputter deposition at room temperature under an argon pressure of 3 mtorr and at a background pressure of $\sim 2.0 \times 10^{-7}$ torr. A thin underlayer of Ta (3 nm) was used to improve adhesion between film and substrate. Films were deposited on two types of substrate: on 100-nm and 200-nm-thick Si_3N_4 membranes used for X-ray magnetic circular dichroism (XMCD) imaging, as well as on thermally oxidized Si wafers used for characterization with vibrating sample magnetometry (VSM).

VSM measurements of the multilayer stack resulted in a saturation magnetization, M_S, of 4.3×10^5 A m^{-1} (per CoFeB volume) and an in-plane saturation field $\mu_0 H_k$ of 0.7 T.

The track structures were patterned with electron beam lithography and lift-off processing. Contact pads were patterned with a second lithography step, followed by the deposition of Ti(5nm)/Au(100nm) bilayers using e-beam evaporation.

The measurements were carried out using scanning transmission X-ray microscopy (STXM) at the MAXYMUS beamline at the BESSY II synchrotron in Berlin, Germany. This technique exploits the XMCD effect that leads to a different absorption of circular polarized X-rays depending on the magnetization structure in the sample. The result is a difference in the transmitted photon intensity, which corresponds directly to the magnetization pattern within the sample (Fig. 1b). The time-resolved measurements were performed in the pump–probe mode of the set-up, allowing us to synchronize the excitation of the sample (pump) with the illuminating X-ray bunches of the synchrotron (probe). This finally ends up in a stroboscopic movie that shows the time-resolved response of the sample in frames. Imaging was performed in the out-of-plane mode, resulting in an orthogonal incidence angle of the circularly polarized X-ray beam that probes the out-of-plane component of the magnetization in the film. Since the technique uses transmitted photons to detect the magnetization pattern, the information about magnetization structures in the film is intrinsically averaged over all layer repetitions.

The Pt/CoFeB/MgO devices were 2 μm wide and 5 μm long. Pump–probe measurements were performed by injecting bipolar current pulses into the track through gold contacts deposited on top. The duty cycle was chosen to be sufficiently low to give the system enough time to cool down during the measurements. The repetition rate of the applied bipolar pulses was ~750 kHz and the length (FWHM) of a single pulse ~5 ns. The mentioned current densities were calculated under the assumption that the amount of current in the MgO layer can be neglected; that is, only the thicknesses of Pt and CoFeB were used to determine the current densities.

The positions of the centres of the skyrmions x_i and y_i were calculated by their centre of mass with the weights $(c - p_i)$, where p_i is the grey value of the corresponding pixel (ranging from 0 to 255) and c is the highest possible grey value (255). The centre of mass of each skyrmion was calculated within the circular mask with a radius of five pixels (for the particular field of view and pixel resolution chosen), which ensures that each skyrmion is fully inside the mask. To minimize the error from the position of the mask with respect to the skyrmion, we shifted the mask to the four nearest neighbouring pixels and the resulting skyrmion position was estimated by averaging the five centre positions to achieve maximal accuracy. The results and error bars were checked by fitting a two-dimensional Gaussian curve to the intensity profile.

Micromagnetic simulations were performed based on the MicroMagnum micromagnetic software, available at http://micromagnum.informatik.uni-hamburg.de, with additional modules for DMI and SOTs developed in our group. To speed up the simulations, we used the effective medium approach introduced in ref. 17. This approach can shrink the whole film with 45 layers into one effective layer, which exhibits the same static and dynamic properties as the full film. The systems were discretized with mesh sizes of $1 \times 1\,nm^2$ and scaled according to the effective medium model. The simulations used a saturation magnetization of 4.3×10^5 A m^{-1}, an exchange constant $A = 1.0 \times 10^{-11}$ J m^{-1}, a Gilbert damping of 0.5 due to the Pt layer, and an out-of-plane uniaxial anisotropy with in-plane saturation field $\mu_0 H_k = 0.7$ T, corresponding to the values measured by VSM. The SOT was included with spin Hall angle $\alpha_H = +0.15$ and a $|\xi|$ of up to 5. All values are given as measured, before applying the effective scaling. The centres of the simulated skyrmions were calculated using the centre of mass with the weights $((M_{z,i} - M_S)/2)$, where $M_{z,i}$ is the z-component of the magnetization in cell i and M_S the saturation magnetization. In agreement with the experimental description given in ref. 31, the SOTs were implemented by adding the torques directly to the explicit LLG equation:

$$\frac{d\mathbf{M}}{dt} = -\frac{\gamma_0}{1+\alpha^2}\mathbf{M}\times\mathbf{H}_{eff} - \frac{\gamma\alpha}{(1+\alpha^2)M_S}\mathbf{M}\times(\mathbf{M}\times\mathbf{H}_{eff}) + \boldsymbol{\tau}_{SOT}$$

The SO torque term $\boldsymbol{\tau}_{SOT}$ then enters as

$$\boldsymbol{\tau}_{SOT} = \frac{\gamma_0}{1+\alpha^2} a_j \left((1+\xi\alpha)(\mathbf{M}\times(\mathbf{M}\times\mathbf{p})) + (\xi-\alpha)M_S(\mathbf{M}\times\mathbf{p})\right)$$

where $\mathbf{p} = \mathbf{e}_j \times \mathbf{e}_z$ is the spin polarization generated by the technical current J and $a_j = (\hbar/2\mu_0 e)(\alpha_H |J|/M_S^2 d)$ is the spin Hall parameter, composed of the spin Hall angle α_H, the amplitude of the applied current, M_S and the thickness d of the magnetic layer. The field-like pre-factor is then effectively given by ξa_j.

Data availability. The data that support the plots within this paper and other findings of this study are available from the corresponding authors upon reasonable request.